Contents list available at CBIORE journal website

International Journal of Renewable Energy Development

Journal homepage: https://ijred.cbiore.id

Research Article

Effect of gurney flaps on the performance of a vertical axis wind turbine under icing condition

Hexiang Yu*, Zhehui Zheng, Pei Yang

Power Mechanical Engineering, School of Energy and Power Engineering, University of Shanghai for Science and Technology, China

Abstract. To investigate the operational characteristics of a vertical-axis wind turbine equipped with Gurney flap blades in icy conditions, the study employs the pitching and sinking movements of an individual blade to replicate the cyclic oscillations experienced by a vertical-axis wind turbine (VAWT) blade during rotation at a temperature of 265K. The aim is to analyze the icing pattern and assess the performance of the wind turbine with varying tip-speed ratios of Gurney flap blades. The findings indicate that as icing time increases, the vertical axis wind turbine experiences a significant decrease in output power. This is attributed to the formation of a leading-edge ice angle, which generates a leading-edge vortex and exacerbates flow separation, consequently reducing the wind turbine's torque coefficient. After 6 minutes of icing, the power coefficient decreases by up to 81%. Additionally, the Gurney flap blades develop ice accumulation on the flaps, which reduces their effectiveness in preventing flow separation. Specifically, when the tip speed ratio of the blade is 3.5, it is observed that the icing on the Gurney flap blades is less effective after 6 minutes compared to that on the VAWT. At a tip speed ratio of 3.5, the vertical axis wind turbine (VAWT) with Gurney flaps ceases to function properly after 6 minutes, leading to a decrease in output power to -0.012. However, within the tip speed range of 1.5 to 3, the Gurney flaps continue to serve as a means of flow control. They enhance the wind turbine's resistance to loss in icing conditions when compared to the original airfoil vertical axis wind turbine under similar operational circumstances.

Keywords: vertical axis wind turbine; Gurney flap icing; dynamic icing; numerical calculation

Received: 25th July 2025; Revised: 16th Oct 2025; Accepted: 6th Dec 2025; Available online: 26th Dec 2025

1. Introduction

In regions with high latitudes and abundant wind, such as mountainous areas and cold plateau, wind turbines are prone to icing during winter due to the combination of lower temperatures and higher humidity (Martini *et al.* 2021). Vertical-axis wind turbines (VAWTs) have the capability to adapt to incoming flows from various directions without requiring yawing devices (Rahman *et al.,* 2021; Wenhao *et al.,* 2021). Moreover, VAWTs are better suited to withstand extreme weather conditions (Islam et al.2013), making them particularly advantageous in cold plateau, mountainous regions (Tahir and Virk 2022). However, the flow field surrounding vertical axis wind turbines (VAWTs) becomes highly complex during operation. The rapid and periodic changes in blade angle of attack necessitate careful consideration of dynamic stall phenomena. Additionally, the icing situation becomes more complex due to the continuously changing inlet conditions.

The impact of icing on the operational state and power generation of vertical-axis wind turbines is a matter of significant concern. Li Yan and colleagues conducted a study examining the aerodynamic behavior of a NACA0018-wing vertical-axis wind turbine across tip speed ratios ranging from 0 to 1. Their investigation involved a combination of wind tunnel experiments and computational simulations. The findings revealed a direct correlation between the increase in tip speed ratio and the increase in icing accumulation, resulting in a significant 37% decrease in wind power coefficient after a 30-minute period of icing. Manatbayev *et al.* (Manatbayev *et al.* 2021); simulated the rotational effects of a wind turbine using the Multiple Reference Frame (MRF) method. The results of the study showed that the power loss of the Vertical Axis Wind Turbine (VAWT) was up to 60% under frost ice conditions. Baizhuma *et al.* (Balduzzi *et al.* 2016); added Slip Mesh (SMT) to the MRF method and considered the non-stationary effects of wind turbine rotation during the calculation of the flow field. The results showed that the power coefficient of the wind turbine decreases by 80% at a temperature of 265 K for a blade tip speed ratio of 1(Gao *et al.,* 2021).

The formation of ice can lead to increased flow separation on the surface of the blades, which in turn reduces the torque and power generated by the wind turbine (Lynch and Khodadoust, 2001). Li Shengmao (Li and Li 2011); and his colleagues conducted a numerical simulation study on the icing phenomenon of the widely used NACA00 (Zhu *et al.,* 2020); airfoil in wind turbines, considering 8 typical angles of attack. The results showed that the maximum ice coverage on the airfoil surface can exceed 30%. Additionally, icing can have a significant impact on the aerodynamic shape and load distribution. Zhang Luting *et al.* (Zhang *et al.* 2011); simulated the static and dynamic flow field of the S809 airfoil with various ice cover patterns. The results indicated that the presence of ice cover on the leading edge of the airfoil altered the distribution of vortices. Furthermore, the ice cover pattern extending towards the suction surface enhanced the development of trailing edge separation vortices. Fu Zhongguang *et al.* (Fu and

* Corresponding author
Email: d15745344515@163.com (H.Yu)

https://doi.org/10.61435/ijred.2026.61538
ISSN: 2252-4940/© 2026.The Author(s). Published by CBIORE

Shi 2016); conducted a study on the flow fields of various ice cover patterns on NACA0012 and S809 airfoils. The results indicated that the growth of the ice cover pattern along the chord has minimal impact on the aerodynamic performance of the airfoils. However, when the ice cover pattern grows towards the suction or pressure surface, it enhances flow separation.

The formation of ice on wind turbine blades can cause damage to their aerodynamic profile, leading to increased flow separation. However, the implementation of Gurney flaps as a straightforward and efficient passive flow control technique can enhance the curvature of the blades and generate a reverse rotating vortex downstream of the flaps. This, in turn, enhances the pressure differential between the upper and lower surfaces of the trailing edge, thereby delaying flow separation. Mayda *et al.* (Mayda *et al.* 2005); installed Gurney flaps (GF) on the trailing edge of the pressure surface of the blade. They found that the GF can increase the airflow folding angle, improving lift. Additionally, the GF can inhibit flow separation and serve as a passive flow control mechanism (Li *et al.,* 2002). Syawitri *et al.* (Syawitri *et al.* 2020); applied the GF to vertical axis wind turbines (VAWT) and demonstrated that the presence of the GF can delay the deep stall of the VAWT blades. This delay eliminates the negative transient moment coefficient and improves turbine performance. Bianchini (Bianchini *et al.* 2019) conducted a study on the impact of Gurney flap placement and height on the performance of vertical-axis wind turbines. The findings indicated that Gurney flaps are effective in delaying blade stall. Installing Gurney flaps with a height of 2% chord length at the trailing edge of the blade pressure surface can significantly enhance wind energy utilization (Cole et al., 2013). Additionally, Zhu Haitian *et al.* (Zhu *et al.* 2020); examined the influence of Gurney flap geometric parameters on the aerodynamic performance of vertical axis wind turbines, revealing a 20.71% increase in the wind turbine's maximum power coefficient.

In brief, the decline in aerodynamic performance of airfoils affected by icing leads to a decrease in the operational efficiency of wind turbines. The implementation of Gurney flaps as a flow control technique has proven effective in enhancing the utilization of wind energy and mitigating flow separation in vertical-axis wind turbines, particularly in non-icing conditions. No previous research has examined the use of Gurney flap configurations on vertical axis wind turbines in ice conditions. Consequently, this study aims to model the functionality of vertical axis wind turbines equipped with Gurney flap blades under icing conditions. The objective of this study is to examine the impact of icing on the effectiveness of Gurney flaps and to provide theoretical insights into the implementation of flow control mechanisms under icing conditions.

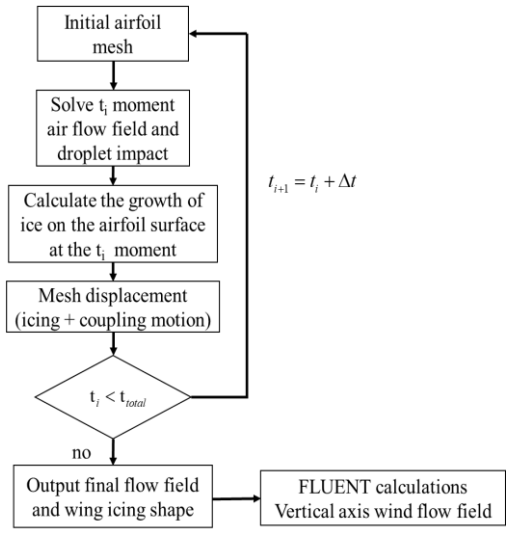

Fig.1. Unsteady simulation framework for oscillating wing icing

2. Calculation model and method

2.1 Calculation of vertical axis wind turbine icing

For vertical axis wind turbine (VAWT) blade icing, it is important to consider the rotational motion of the turbine. Only considering icing at a fixed angle of attack would overlook the icing characteristics at different angles of attack and the destabilizing effect caused by rotation. Due to the limitations of the FENSAP-ICE software, it is not possible to directly simulate the transient icing process of a vertical axis wind turbine. Hence, this study incorporates icing calculations to induce both pitching and sinking motions in the airfoil (Brunner *et al.*, 2022; Tsai and Colonius, 2016). The aim is to more accurately represent the fluctuation in the asymmetric angle of attack experienced by the blade during vertical axis wind turbine operation. The unsteady icing during blade movement is computed using the three-phase flow module of FENSAP-ICE. Subsequently, the calculated icing shape is applied to the vertical axis wind turbine, and the Fluent software is used to conduct a numerical simulation of the turbine's flow field. The computational flow is depicted in Figure 1.

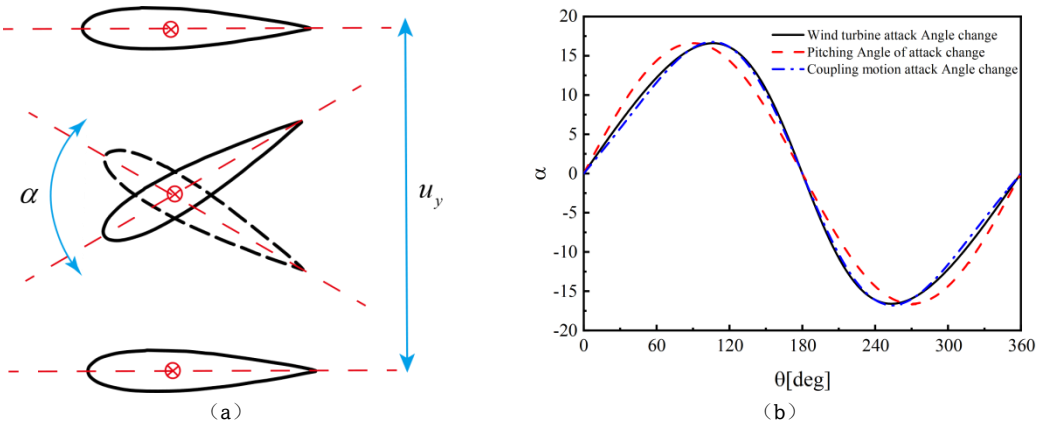

Fig.2. Blade motion and angle-of-attack variation: (a) blade motion method; (b) coupled motion angle-of-attack change at TSR = 3.5.

The motion of the blade is shown in Fig.2a, with the pitching motion oscillating around the rotation axis at a distance of 0.25c from the leading edge, and the sinking motion being up and down reciprocating in the direction perpendicular to the incoming flow. The expressions of the angle of attack variation for sinusoidal oscillation, coupled motion, and vertical axis wind turbine are given in Eq. (1) ~(3). Fig.2b shows the comparison of the angle of attack variation for the three modes of motion at TSR=3.5. It can be seen that the wing motion method used in this paper can better simulate the angle of attack variation during the operation of the wind turbine.

$$\alpha(t)=\alpha_t-\alpha_0=\alpha_m\sin(2\pi f_1 t)-\tan^{-1}\frac{u_y}{U_\infty}=\alpha_m\sin(2\pi f_1 t)-\tan^{-1}(\frac{u_m sin(4\pi f_1 t)}{U_\infty}) \quad (1)$$

Substituting$f_1=\frac{\lambda U_\infty}{2\pi R}$ into equation (1) gets：

$$\alpha(t)=\alpha_t-\alpha_0=\alpha_m sin\left(\frac{\lambda U_\infty}{R}t\right)-tan^{-1}(\frac{u_m}{u_\infty}\cdot sin(\frac{2\lambda U_\infty}{R}t)) \quad (2)$$

$$\alpha=tan^{-1}\left(\frac{sin\,\theta}{\lambda+cos\,\theta}\right) \quad (3)$$

where α_t is the pitch motion angle of attack, α_m is the pitch motion angle of attack amplitude, α_0 is the wing relative to the incoming flow angle of attack during the sink motion, f_1 is the pitch motion oscillation frequency, R is the wind turbine rotation radius, u_y is the sink motion speed, U_∞ is the incoming flow speed, u_m is the sink motion speed amplitude, t is the oscillation time, is the wind turbine blade azimuth, and $\lambda$is the wind turbine blade tip speed ratio.

2.2 Air-droplet two-phase flow solution

The Fensap solver solves the mass, momentum, and energy conservation equations using partial differential equations, and the control equations are shown in (4) to (8). In the equation, the subscript g represents air and the subscript p represents droplet particles, The time derivative term uses the Arbitrary Lagrangian-Eulerian (ALE) formula and the terms to the right of the equal signs in Eqs. (5) and (7) represent the effect of air on the droplet and the droplet on the air. In the calculation, air and droplets are solved together in time. Eq. (4) represents the continuity equation of the carrier air phase, while Eq. (5) is the corresponding momentum equation, including the interphase source terms due to drag and pressure forces between air and droplets. Eq. (6) denotes the total energy conservation for the air phase. Eqs. (7) and (8) describe, in a volume-averaged form, the transport of momentum and energy of the dispersed droplets, where the source terms account for the exchange of momentum and heat with the surrounding air.

$$\frac{d(\rho_g)}{dt}-\frac{dx_k}{dt}\frac{\partial(\rho_g)}{\partial x_k}+\frac{\partial(\rho_g V_{g,i})}{\partial x_i}=0 \quad (4)$$

$$\frac{d(\rho_g V_{g,i})}{dt}-\frac{dx_k}{dt}\frac{\partial(\rho_g V_{g,i})}{\partial x_k}+\frac{\partial(\rho_g V_{g,i}V_{g,k})}{\partial x_k}=\vec{\nabla}p_g+\vec{\nabla}\cdot(\vec{\tau}_g)+\rho_g\vec{g} \quad (5)$$

$$\frac{d(a_p)}{dt}-\frac{dx_k}{dt}\frac{\partial(a_p)}{\partial x_n}+\frac{\partial(a_p V_{p,j})}{\partial x_i}=0 \quad (6)$$

$$\frac{d(V_{p,j})}{dt}-\frac{dx_k}{dt}\frac{d(V_{p,j})}{\partial x_k}+V_{p,k}\frac{\partial(V_{p,j})}{dx_n}=(1-\frac{\rho_g}{\rho_p})\bar{g}+\frac{3}{4}\frac{1}{\rho_p}C_D\frac{\mu_g}{D_{p2}}\mathrm{Re}_p(\vec{V}_g-\vec{V}_p) \quad (7)$$

$$\frac{\partial\rho_a E_a}{\partial\tau}+\vec{\nabla}\cdot(\rho_a\vec{V}_a H_a)=\vec{\nabla}\cdot(\kappa_a(\vec{\nabla}T_a)+v_i\tau^{ij})+\rho_a\vec{g}\cdot\vec{V}_a \quad (8)$$

Droplet collection efficiency is calculated as shown in Eq. (9):

$$\beta=\frac{\alpha_d v_d\cdot\vec{n}}{V_\infty} \quad (9)$$

Where α_d is the droplet volume fraction and v_d is the droplet velocity. Thus, Eq. (9) defines the local collection efficiency β as the ratio between the droplet mass flux impinging on the blade surface and the freestream droplet mass flux, and it characterizes how effectively the moving airfoil captures supercooled droplets under a given flow condition.

2.3 Calculation of ice accumulation shapes

For icing calculations, Fensap adds the Messinger model to the unsteady air-droplet two-phase flow model to calculate the ice accumulation rate and to move the grid of the icing surface in time. The icing part solves two partial differential equations for mass conservation and energy conservation as shown in Eq. (10) and Eq. (11). The three terms on the right side of the momentum equation correspond to the mass transfer, evaporation and ice growth. The terms on the right side of the energy conservation equation are the kinetic energy of the impacting water droplet, the fusion latent heat, the evaporation latent heat, the sublimation latent heat, and the radiation and convection cooling latent heat, respectively.

$$\rho_f[\frac{\partial h_f}{\partial t}+\vec{\nabla}\cdot(\vec{u}_f h_f)]=V_\infty LWC\beta-\dot{m}_{\mathrm{evap}}-\dot{m}_{\mathrm{ice}} \quad (10)$$

$$\rho_f\left[\frac{\partial h_f c_f\tilde{T}}{\partial t}+\vec{\nabla}\cdot\left(\vec{V}_f h_f c_f\tilde{T}\right)\right]=\left[c_f\tilde{T}_{d,\infty}+\frac{\vec{u}_d{}^2}{2}\right]V_\infty LWC\beta-0.5(L_{evap}+L_{subl})\hat{m}_{evap}+\left(L_{fus}-C_{ice}\tilde{T}\right)\dot{m}_{ice}+\sigma\varepsilon(T_\infty^4-T^4)+\dot{Q}_h \quad (11)$$

The generation of backflow water is explained by the velocity vector of the water film, using the linear velocity distribution of the water film as the velocity of the water film on the blade surface, as in Eq. (12).

$$\vec{V}_f(\vec{x},y)=\frac{y}{\mu_f}\vec{\tau}_{a,wall}(\vec{x}) \quad (12)$$

where $\vec{\tau}_{a,wall}$ is the shear stress of air, is the main driving force of the wall water film movement.

The liquid film thickness h_f, the equilibrium temperature at each phase intersection T_f, and the instantaneous icing mass $m_{ice}$are determined by the set of equations in Eq. (13). These inequalities ensure that the model predicts the absence of liquid water when the equilibrium temperature is below the freezing point (0 °C) and the absence of ice when there is a film above 0 °C.

$$\begin{cases}h_f\geq 0\\ \dot{m}_{ice}\geq 0\\ h_f T_f\geq 0\\ m_{ice}\tilde{T}_f\leq 0\end{cases} \quad (13)$$

The icing thickness on the blade surface is determined by Eq. (14), and since this study uses a two-dimensional model, the length should be used instead of the area.

$$h_{ice} = \frac{\dot{m}_{ice} \Delta t \Delta A}{\rho_{ie}} \quad (14)$$

In order to quantitatively analyse the icing characteristics of the blade surface, the icing area ratio (NIAR), the upper limit of icing (η_{Lu}) and the lower limit of icing (η_{Ld}) are introduced, defined by Eq.(15)–(17).

$$\text{NIAR}=\frac{A_{ice}}{A_{blade}} \quad (15)$$

$$\eta_{L_u} = \frac{L_u}{c} \quad (16)$$

$$\eta_{L_d} = \frac{L_d}{c} \quad (17)$$

Where A_{ice} represents the net icing area of the blade surface in mm^2 A_{blade} denotes the cross-sectional area of the blade in mm^2; L_u stands for the limiting chordal position of the upper surface in mm; L_d refers to the limiting chordal position of the lower surface in mm; and c represents the chordal length of the blade in mm.

2.4 Computational domain and mesh sensitivity analysis

2.4.1 Blade coupled motion icing model

Icing calculations for vertical axis wind turbines were conducted using the ANSYS-FENSAP-ICE commercial software for icing simulation and analysis. The computational domain, as depicted in Figure 3a and the grid distribution near the airfoil is shown in Figure 3b, involved coupled motion icing calculations, with the center of rotation positioned at a distance of 0.25c from the leading edge of the NACA0018 airfoil. The radius of the computational domain was 20c, and the mesh resolution of the airfoil extended to approximately 3c. The icing calculations in this study employed the SA turbulence model, with far-field Riemann boundary conditions used for the computational domain. The airfoil surface acts as a boundary with no-slip conditions. A non-stationary analysis of the two-phase flow, which involves air and liquid droplets, is conducted using a dual time-step method. This approach involves setting the physical time-step and total solution time and performing a sufficient number of pseudo-time iterations at each time-step to achieve solution convergence. In this investigation, the physical time-step is determined according to Equation (18) to ensure the accuracy of the computation.

$$\Delta t = \frac{t_{period}}{\Delta \alpha} \quad (18)$$

Where Δt is the physical time step, t_{Period} is the time for one cycle variation of the angle of attack, and $\Delta \alpha$ is the amount of angle of attack variation in one cycle.

To ensure the accuracy of the calculation, the lift coefficient of the airfoil was evaluated at a flow velocity of 9.3 m/s and an angle of attack of 10°. Additionally, a mesh sensitivity analysis was conducted, primarily involving changes to the first layer height of the mesh on the airfoil surface and the number of nodes on the airfoil surface. The results of this analysis are illustrated in Figure 3c. As the number of grids increases, the variation in the lift resistance coefficient gradually decreases. Considering the cost and accuracy of the calculation, a final grid number of 256,000 is selected for the icing calculation.

2.4.2 Computational Modelling of Vertical Axis Wind Turbines

The two-dimensional model is capable of accurately replicating the flow in the central plane when the vertical axis wind turbine has a high aspect ratio (Bianchini *et al.*, 2017). This approach is employed in the present study to minimize the computational resources required for simulating icing on vertical axis wind turbines. The geometric parameters of the vertical axis wind turbine were obtained from the literature (Wang and Zhuang, 2017). The simulation data for the wind turbine, presented in Table 1, was organized within a computational domain of 35D×20D. The boundary conditions and computational domain are depicted in Figure 4a. To simulate the rotation of the wind turbine, a sliding mesh was employed, and the mesh near the airfoil was refined. The initial layer of the mesh had a height of 0.02 mm, resulting in a maximum y+ value of 1.96 at the wall. The mesh distribution is illustrated in 4b–4d. The calculations use the SST k-ω turbulence model (Daróczy *et al.*, 2015). The pressure-velocity coupling method is in SIMPLE format. The time and spatial discretization is second-order windward. The non-constant physical time step is taken as an azimuthal increment of 1°. The results are obtained from the last cycle after 20 cycles, when the difference between two consecutive cycles has been neglected.

Table 1
Vertical axis wind turbine simulation data

Airfoil section	NACA0018
Chord length (m)	0.12
Wheel Diameter,D(m)	1
Blade number,N	2
Axis Diameter(m)	0.04
Free-stream velocity(m/s)	9.3
Flap height (mm)	3.6

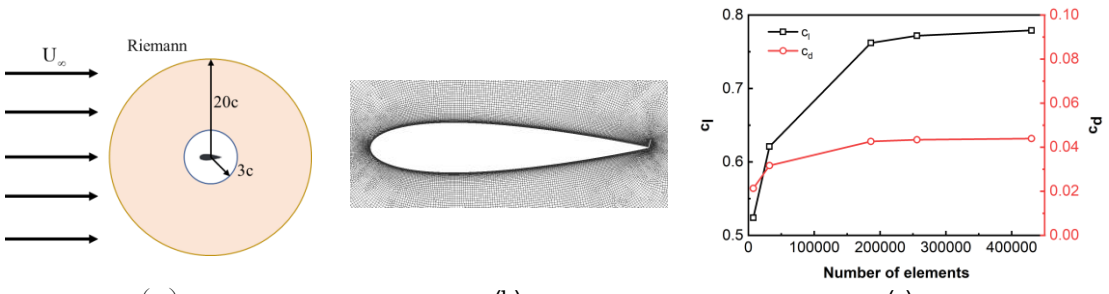

（a） (b) (c)

Fig.3. Coupled-motion icing model and mesh: (a) computational domain; (b) mesh near the wing; (c) mesh sensitivity analysis for different grid resolutions.

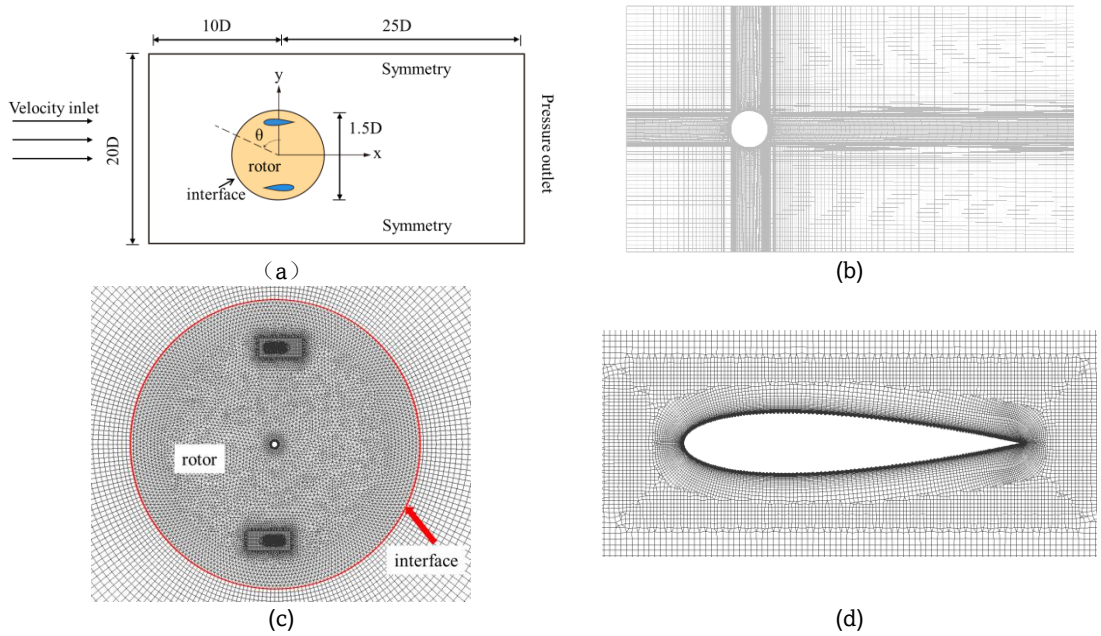

Fig.4. Computational domain and mesh distribution of the vertical axis wind turbine: (a) computational domain; (b) static domain mesh; (c) rotational domain mesh; (d) mesh near the wing.

Table 2
Mesh solution

	Stationary domain	rotation domain	Total number of meshes	y+	Cp
1	5.4W	17.8W	23.2W	4.26	0.468
2	5.4W	36.2W	41.6W	1.96	0.446
3	11.4W	36.2W	47.6W	1.96	0.439
4	22.8W	41.5W	64.3W	1.18	0.437
5	22.8W	62.03W	14.83W	0.62	0.436

To evaluate grid independence, the power coefficients obtained from comparing five grid sets with different resolutions for a leaf tip speed ratio of 2.5 are presented in Table 2. Define the power coefficient:

$$Cp = \frac{M\omega}{\rho U_{\infty}^{3} r} \quad (19)$$

Where M represents the output torque of the vertical axis wind turbine in N/m; ω is the rotation speed of the wind turbine in rad/s; ρ is the density of air in kg/m3; U_{∞} is the free-flowing speed in m/s; and r is the radius of the wind turbine in mm.

The torque coefficients were determined using the following calculation method:

$$Cm = \frac{M}{0.5\rho U_{\infty}^{2} A} \quad (20)$$

Where M is the output torque of the vertical axis wind turbine, ω is the wind turbine rotation speed, ρ is the air density, U∞ is the free incoming flow speed and r is the wind turbine, consistent with the definitions used for the power coefficient.

In Table 2, it is evident that the power coefficients show a tendency to stabilize as the number of grids increases. Taking into consideration both computational accuracy and time efficiency, this study chooses to use the third grid scheme.

3 Validation

3.1 Icing shape verification

Fouladi (Fouladi *et al.,* 2015) and Reinert (Reinert *et al.,* 2011) conducted computational simulations and experiments of oscillatory icing on SC2110 airfoils, using the specific icing parameters detailed in Table 3. To validate the accuracy of the ice formation pattern obtained from the non-stationary icing simulation method utilized in this study, the ice pattern generated through the simulation is compared with experimental data using the computational approach detailed in this paper, carried out under the same airfoil and icing conditions. The comparative results are depicted in Figure 5. The findings of this study show a strong agreement between the simulation outcomes presented here and the ice patterns derived from previous simulations documented in the literature (Fouladi *et al.,* 2015), as well as with the experimental ice patterns reported in the literature (Fouladi *et al.,* 2015). The difference in maximum icing thickness at the leading edge is mainly due to potential variations in the droplet size distribution used in the simulation, compared to the conditions in the experimental setup. Consequently, the same simulation

Table 3
Experimental icing parameters

Description	Rime icing condition	Glaze icing condition
Airfoil section	SC2110	SC2110
Chord length (m)	0.381	0.381
Pitch frequency(Hz)	2.8	2.8
Angle of attack range (°)	5±6	5±6
Free-stream velocity(m/s)	77.17	77.17
Ambient pressure (Pa)	101325	101325
Ambient temperature (℃)	-14	-14
MVD (μm)	22	22
LWC (g/m3)	0.5	1
Total icing time(s)	180	180

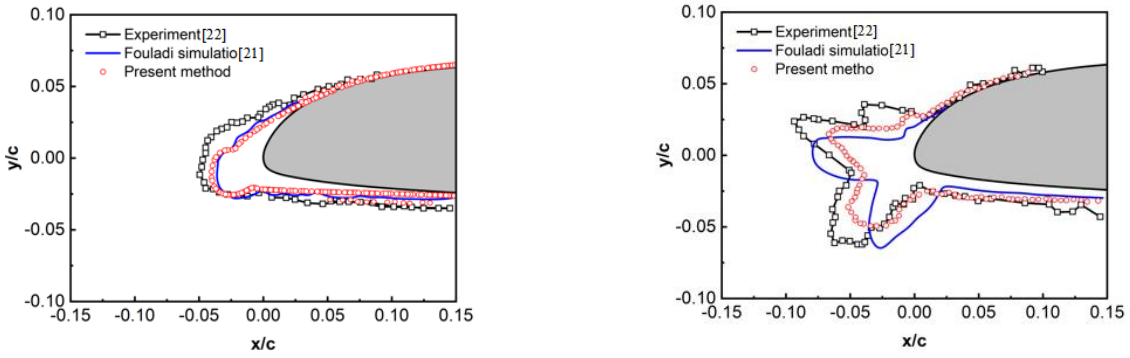

Fig.5. Oscillatory icing patterns on the SC2110 airfoil under two icing regimes: (a) rime icing condition; (b) glaze icing condition.

methodology will be used for the integrated kinematic icing calculations.

3.2 Wind turbine aerodynamic performance verification

In order to validate the calculation method for the two-dimensional vertical axis wind turbine model, the present study compares the simulated values with the experimental results (Tescione *et al.,* 2014) and numerical simulation result s (Rezaeiha *et al.,* 2019) of the flow-normalized velocity distribution on various wake cross sections (Tescione *et al.,* 2014). The wind turbine model used an airfoil with a chord length of 0.06 m and maintained other geometric parameters as outlined in this paper. Figures 6a and 6b illustrate the normalized velocity distribution of the flow direction on the x/R=2 and x/R=3 cross sections at TSR=4.5, respectively. The comparison reveals a close correspondence between the simulated values in this paper and those reported by Rezaeiha

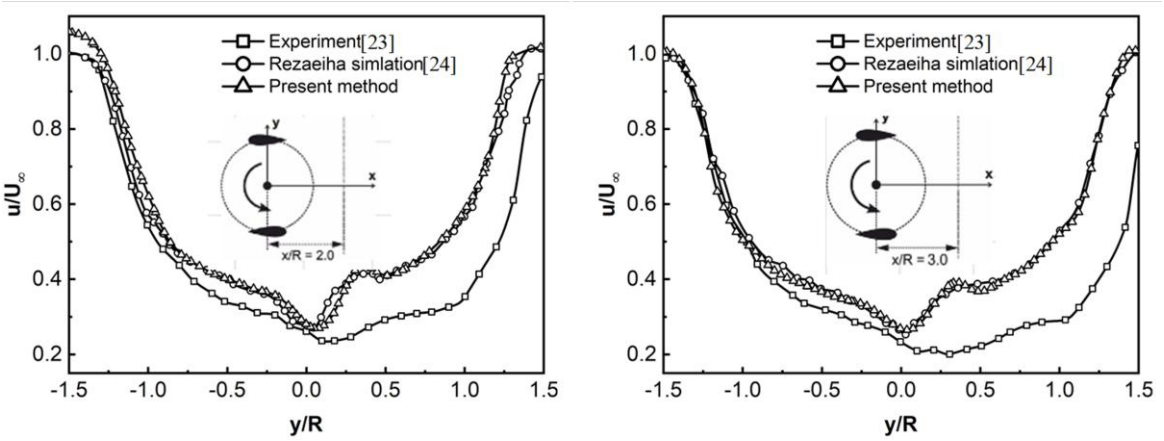

Fig.6. Normalized streamwise velocity at different downstream sections for TSR = 4.5: (a) x/R = 2; (b) x/R = 3.

Table 4
Vertical axis wind turbine validation calculation parameters

Description	Conditions
Airfoil section	NACA0018
Chord length, C(m)	60
Wheel Diameter, D(mm)	1000
Blade number, N	2
TSR	4.5
Free-stream velocity , V_∞(m/s)	9.3

(Rezaeiha *et al.,* 2019). Discrepancies in the 3D vertical axis wind experimental values (Tescione *et al.,* 2014) are attributed to the exclusion of components with poor aerodynamic performance, such as the support arms, and the limitations of the 2D simulation in addressing blade end losses. The discrepancies between the experimental and vertical axis wind force values can be attributed to the oversight of components with poor aerodynamic performance, such as support arms, and the failure of the 2D simulation to account for blade end losses.

4. Results and Discussion

4.1 Airfoil icing analysis

The parameters for calculating icing on a vertical-axis wind turbine equipped with Gurney flaps were selected based on the existing literature on icing conditions (Feng *et al.,* 2012). To speed up the visualization of icing shapes and reduce computational costs, the specific icing conditions used in this study are outlined in Table 5.

Figure 7 illustrates the spatial arrangement of ice formation on the vertical axis wind turbine blades and Gurney flap blades at a temperature of 265 K. When glaze icing is present, the impact of water droplets on a blade is affected by the relatively high ambient temperature, which prevents immediate freezing and leads to the formation of a water film. The film is affected by the movement of the blade and pressure gradient, causing it to shift to the sides and gradually condense into ice. As a result, ice convexities and ice angles form on the blade's surface. Furthermore, as the tip speed ratio of the blade increases, the ice concentration on the leading edge also increases, resulting in a rougher leading edge shape due to the accumulation of ice. The ice puddles were more noticeable on the inner side of the blade than on the outer side, and the ice was slightly thicker on the inner leading edge of the blade compared to the outer edge.

After installing Gurney flaps, there is minimal change in the formation of ice at the leading edge at a tip speed ratio of 1.5. As the tip speed ratio increases, the angle of ice formation at the leading edge of the Gurney flap blades becomes more pronounced compared to the original blade icing configuration. The presence of flaps causes ice to accumulate at the trailing edge of the blade. The flaps' impact on the airflow near the blade results in the formation of a vortex structure in front of the flaps, displacing water droplets near the root of the flap. This results in an inverted triangular shape of icing, with a smaller icing area near the root of the flap and concentrated icing at the top of the flaps.

To quantitatively analyse the icing characteristics of the blade surface, the icing area ratio (NIAR) and the icing limits xu and xl defined in Section 2.3 are used. At a temperature of 265 K, the net ice coverage on the blade surface is illustrated in Figure 8. At 265 K, the increase of NIAR with TSR results from higher relative inflow and more droplets intercepted per unit time by the pitching schedule. The initial 3-min reduction of NIAR on the GF blade stems from flap-induced pressure redistribution and delayed attachment near the trailing edge; by 6 min, roughness growth and local blockage around the flap tip enhance recirculation and droplet residence, raising GF-blade NIAR above the baseline. As the blade tip speed ratio increases, the relative wind speed acting on the blade also increases. This allows the pitching motion of the blade to capture more water droplets per unit time, resulting in a greater accumulation of ice within the same icing duration. Compared to the unmodified airfoil, the icing coverage on the Gurney flap blades is slightly reduced at the 3-minute mark, indicating a slower rate of ice accumulation during the initial stages of icing. However, when the icing duration extends to 6 minutes, the icing coverage on the Gurney flap blades exceeds that of the original airfoil.

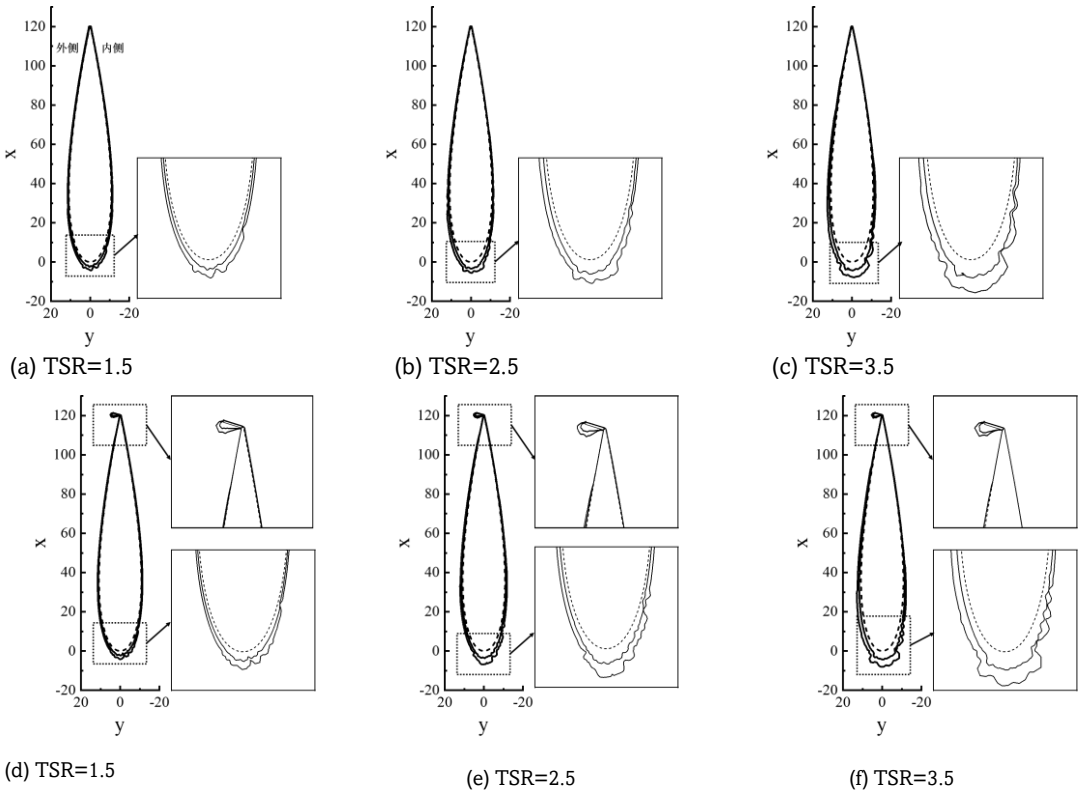

Fig.7. Surface icing distribution of the original blade (a–c) and the Gurney flap blade (d–f) at 265 K for different tip speed ratios: (a), (d) TSR = 1.5; (b), (e) TSR = 2.5; (c), (f) TSR = 3.5.

Table 5
Wind turbine blade icing conditions

Description	Glaze icing condition
Free-stream velocity(m/s)	9.3
Ambient temperature (K)	265
MVD (μm)	40
LWC (g/m3)	2.32
TSR	1.5~3.5
Total icing time(min)	3、5

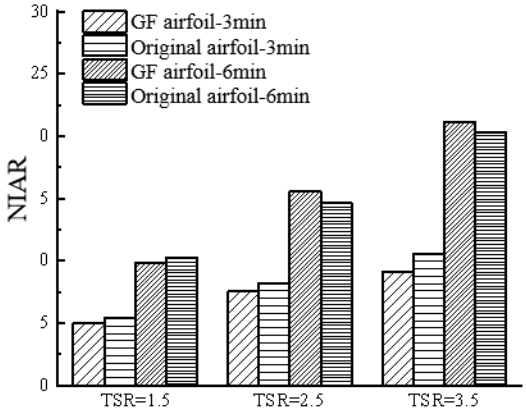

Fig.8 Net icing area ratio of blade surface at 265K temperature

Figures 9a and 9b give the variation of the upper and lower limits of icing for the original and Gurney flap blades for different tip speed ratios and different icing times. From the figure, it is evident that the position of the icing limit is primarily influenced by the tip speed ratio, which shows minimal variation at different icing times. Ice accumulation covers almost the entire airfoil profile for the original blade at tip speed ratios (TSR) less than 2.5, and the location of the icing limit shifts toward the leading edge as the tip speed ratio increases. The Gurney flap blade experiences reduced icing coverage on its upper surface because a vortex forms near the trailing edge of the flap. The upper limit position of blade icing shows minimal variation under different operational conditions, typically ranging from 0.9 to 0.95. Furthermore, the amount of icing on the lower surface of the Gurney flap blade is greater than that observed on the original blade. As the tip speed ratio increases, the range of variation of the angle of attack decreases, and the icing limit positions all gradually move towards the leading edge. This leading-edge shift agrees with the TSR-driven migration of the stagnation point and the reduced amplitude of instantaneous angle of attack. For GF blades, the flap-induced trailing-edge vortex weakens upper-surface accretion but increases lower-surface impingement, explaining the observed asymmetry of the icing limits.

4.2 Performance Analysis of a Vertical Axis Wind Turbine Under Icing Conditions

To assess the influence of icing on the operational efficiency of a vertical axis wind turbine, an analysis was carried out to compare the power and torque characteristics of the turbine under icing conditions and without. The torque coefficients are calculated using the definition given in Section 2.4.2.

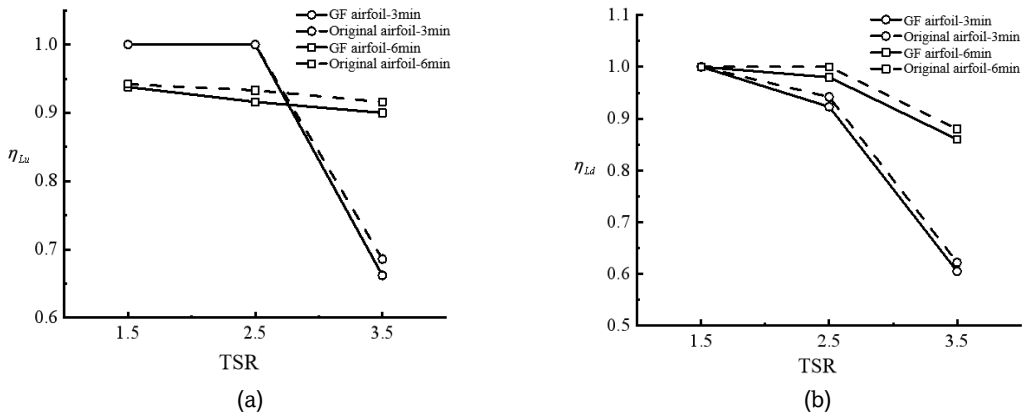

Fig.9. Icing limits of the original and Gurney flap blades at different tip speed ratios and icing times: (a) upper surface icing limit; (b) lower surface icing limit.

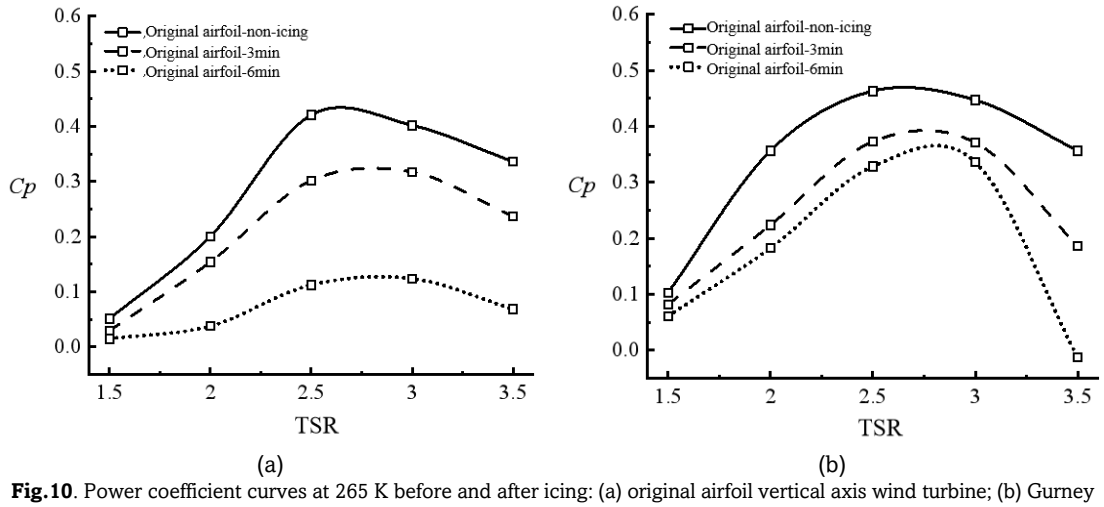

Fig.10. Power coefficient curves at 265 K before and after icing: (a) original airfoil vertical axis wind turbine; (b) Gurney flap vertical axis wind turbine.

The power coefficient curves for the original vertical axis wind turbine with wing type and the vertical axis wind turbine with Gurney flaps at a temperature of 265 K are presented in Figures 10a and 10b, both before and after icing. This "rise–then–fall" Cp behavior with increasing TSR is consistent with prior VAWT studies (Rezaeiha *et al.,* 2018). The power coefficients of both wind turbines show a pattern of increasing and then decreasing with the increase in tip speed ratio. The optimal operational conditions are observed to be near a tip speed ratio of 2.5. Furthermore, the incorporation of Gurney flaps has led to a significant improvement in the power coefficients of the wind turbines.

As icing time increases, the power coefficient under each blade tip speed ratio decreases to varying degrees. For the original wing-type vertical axis wind turbine, when the icing time reaches 6 minutes, the power coefficient decreases to a lower level. The maximum power coefficient, equal to 0.124, occurs when the blade tip speed ratio is 3. At this point, the wind turbine is unable to operate normally. The Gurney flap vertical-axis wind turbine demonstrates improved power characteristics following icing. With prolonged icing, the turbine can maintain higher output power at tip speed ratios below 3, reaching a maximum power coefficient of 0.317 at a tip speed ratio of 3. However, at tip speed ratios exceeding 3, icing leads to a rapid decline in the power coefficient of the Gurney flap vertical axis wind turbine. After 6 minutes of icing, the power coefficient decreases to -0.012 at a blade tip speed ratio of 3.5, making the wind turbine inoperable at this point. This trend agrees with Gurney-flap literature: lift gains accompany increased drag and separation sensitivity at higher loading (Bianchini *et al.,* 2019, Jang *et al.,* 1992). Comparable icing-induced power losses have been reported in field and modeling studies of wind turbines (Gao *et al.,* 2021). The Cp loss under icing combines increased profile drag from roughness/ice horns with a reduced lift-curve slope due to premature separation and dynamic stall. For GF blades, icing around the flap tip weakens separation control and widens the negative-torque sector at high TSR, explaining the rapid Cp drop beyond TSR≈3. At TSR≤3, the flap still delays trailing-edge separation enough to maintain a higher Cl/Cd and thus a higher Cp than the baseline for the same icing duration.

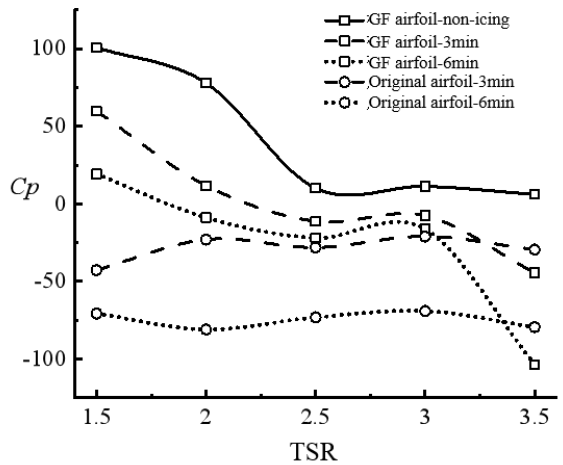

Fig.11 Power factor change rate at 265K temperature

The variation of power coefficients for each icing condition are analyzed by comparing them to the original airfoil-type vertical-axis wind turbine, which serves as a baseline, as shown in Figure 11. The enhancement in the power coefficient of the wind turbine resulting from the addition of Gurney flaps decreases as the tip speed ratio increases in non-icing conditions. The maximum improvement of 100.6% is achieved at a tip speed ratio of 1, while at the optimal operating condition with a tip speed ratio of 2.5, the power coefficient is increased by 10.1%.

After applying ice to a vertical axis wind turbine with a basic airfoil design, the rate of decrease in power coefficient shows less variation across different blade tip speed ratios for the same duration of icing. After being iced, the Gurney flap vertical axis wind turbine demonstrates improved anti-icing performance, with a smaller decrease in power coefficient at tip speed ratios less than or equal to 3. The power coefficient of the Gurney flap wind turbine decreases more when the tip speed ratio is 3.5 for the same icing time. The Gurney flap vertical-axis wind turbine continues to demonstrate higher power coefficients compared to the un-iced original airfoil after being subjected to icing for 3 minutes at tip speed ratios of 2 or less. However, when the icing duration extends to 6 minutes, the iced Gurney flap vertical-axis wind turbine only exhibits higher power coefficients than the original airfoil without icing at tip speed ratios of 1.5. Furthermore, for the same icing durations, the Gurney flap vertical-axis wind turbine achieves higher power output when the tip speed ratio is below 3.5. This suggests that employing iced-up Gurney flaps can improve the performance of wind turbines under a wide range of operating conditions.

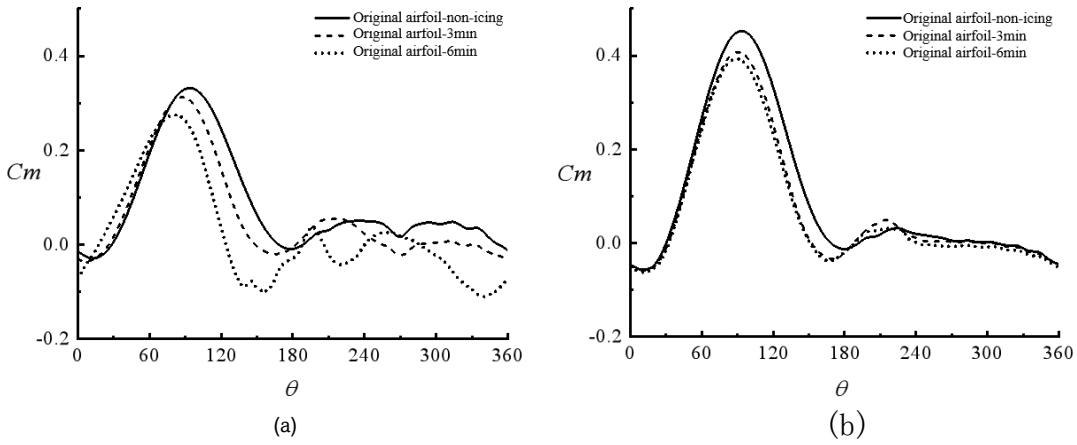

Fig.12. Single-blade moment coefficient at TSR = 2.5: (a) original airfoil vertical axis wind turbine; (b) Gurney flap vertical axis wind turbine.

To conduct a more comprehensive analysis of the impact of blade icing on the aerodynamic properties of wind turbines, the single blade moment coefficient of the wind turbine is calculated. This analysis focuses on determining the optimal operational conditions for the original wing-type vertical axis wind turbine with a tip speed ratio of 2.5, as well as the operational conditions for negative power of the Gurney flap vertical axis wind turbine when the tip speed ratio is 3.5. Figure 12 illustrates the moment coefficient of a single blade of a wind turbine with a tip speed ratio of 2.5. In the case of the original airfoil type vertical axis wind turbine, the azimuth angle at which the moment coefficient reaches its peak shifts from 95° to 82° as the icing time increases. This forward shift indicates earlier leading-edge separation triggered by the suction-side ice horn, shrinking the effective positive-torque window. The pre-peak rise reflects transient circulation build-up before stall, whereas the post-peak deficit is dominated by enlarged separation and wake interference. Following icing, there is a slight increase in the moment coefficient before reaching the peak, and a substantial decrease in the moment coefficient in the remaining windward and leeward areas after reaching the peak. This decrease is attributed to the intensified flow separation at the leading edge caused by icing. After subjecting the Gurney flap vertical axis wind turbine to icing, there was a reduction in both the moment coefficients and peak moment coefficients, particularly in the windward region. Additionally, the moment coefficients exhibited a more gradual fluctuation in the leeward region.

Figure 13 depicts the moment coefficient curve at a tip speed ratio of 3.5. It is evident that the azimuth angle of the peak moment coefficient shifts forward after icing of the original airfoil with an increase in icing time. Additionally, the moment coefficient in the windward area decreases, and a second positive peak moment occurs at an azimuth angle of 180°~240° for 6 minutes. After applying ice to the Gurney flap vertical axis wind turbine, a similar bimodal fluctuation was observed at the 6-minute mark of the icing process. However, the peak moment in the leeward region continued to show a negative value. Furthermore, when compared to a tip speed ratio of 2.5, the Gurney flap vertical axis wind turbine shows a wider range of negative moment regions and higher negative moment values at a tip speed ratio of 3.5, even before icing occurs. As the duration of icing increases, the average moment coefficient of the blade operation over a week experiences a substantial decrease due to the significant reduction in the range and magnitude of the positive moment coefficient. At an icing time of 6 minutes, the average moment coefficient reaches -0.0052, leading to a significant decrease in the wind turbine power coefficient.

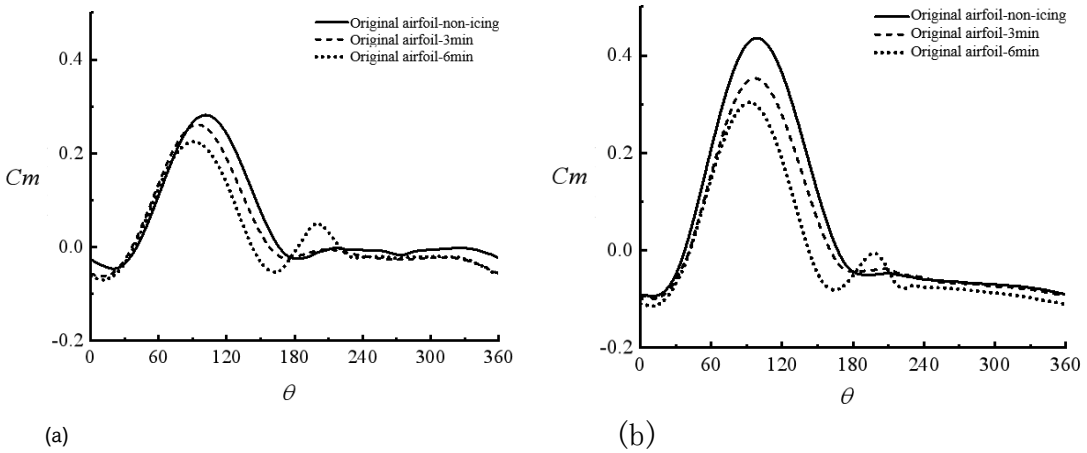

Fig.13. Single-blade moment coefficient at TSR = 3.5: (a) original airfoil vertical axis wind turbine; (b) Gurney flap vertical axis wind turbine.

4.3 Analysis of wind turbine flow field under icing Conditions

To examine the effect of icing on the airflow around a vertical axis wind turbine, an analysis was performed on the vortex cloud and streamline diagrams depicting the turbine blades at different azimuthal angles. This analysis is conducted for icing durations of 6 minutes, with the turbine operating at tip speed ratios of 2.5 At a tip speed ratio of 2.5, Figure 14a depicts the vortex cloud and flow distribution at a 90° azimuth angle. At this particular tip speed ratio, the original airfoil leads to the formation of separating vortices at the leading edge of the suction surface, caused by the development of high angles on both sides of the blade. Additionally, the range of trailing edge vortices and the flow separation region increases, resulting in a decrease in the peak moment at this specific azimuthal angle. At this time, the ice formation at the leading edge of the Gurney flap blades did not develop towards the suction surface, thus no leading edge vortex was generated after icing. However, its ability to suppress the trailing edge flow separation was weakened, and the range of the reverse vortex formed downstream of the flap increased. This increase of reverse-vortex extent and the associated suction loss under icing are consistent with iced-airfoil aerodynamics and with Gurney-flap flow control limits at higher loading (Bragg et al., 2005, Bianchini *et al.,* 2019, Jang *et al.,* 1992).The enlarged reverse vortex lowers suction recovery and adds pressure drag near the flap, directly reducing the peak torque at 90°. This flow–force linkage explains the observed drop of the single-blade moment and the associated Cp deficit under icing.

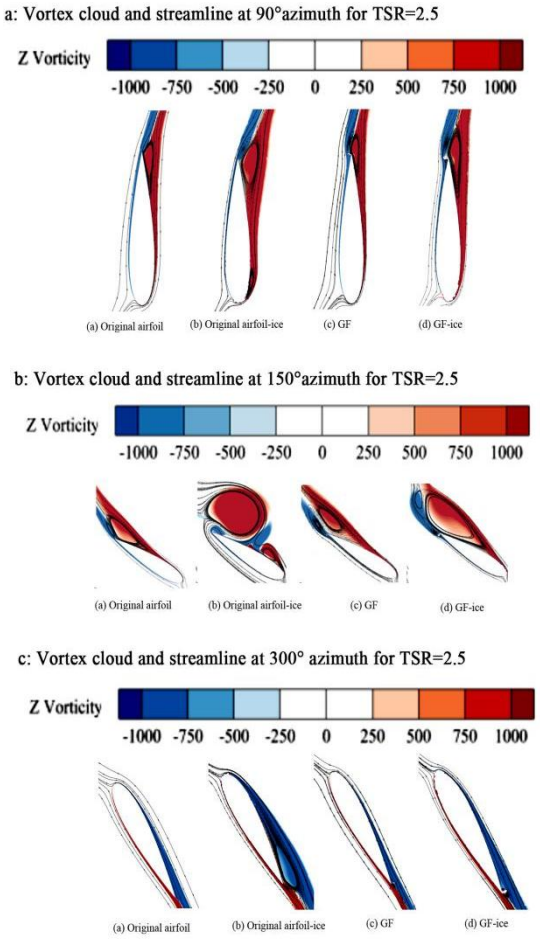

Fig. 14 Vortex clouds and streamlines at azimuth angles 90°, 150°, and 300° for TSR = 2.5.

The flow pattern around the blade at an azimuth angle of 150° is illustrated in Figure 14b. In contrast to the flow separation at the trailing edge in the absence of icing, the formation of a leading-edge vortex due to the presence of ice on the original airfoil's leading edge persists at this azimuth angle. This results in the formation of a wide range of stall vortices and secondary vortices in the suction plane, gradually detaching from the trailing edge. During this detachment process, a trailing edge vortex is generated at the trailing edge by the pressure side of the suction plane, resulting in significant dynamic stall and a consequent notable decrease in the torque coefficient. The observed behavior matches classic descriptions of dynamic-stall onset driven by leading-edge separation on oscillating (and iced) airfoils (Bragg *et al.,* 2005, McCroskey, 1981). The LEV growth paired with trailing-edge shedding forms a vortex couple that persists into the downstroke, extending the negative-torque sector. This persistence clarifies the phase lag of aerodynamic loading and the Cp loss at higher TSR.

The flow pattern around the blade at a 300° azimuth is illustrated in Figure 14c. In the downwind area, icing on the original airfoil causes the flow to separate more at the trailing edge and generates a wider range of vortices. Consequently, the moment coefficient decreases in the downwind region. Additionally, there is minimal change in the flow field before and after the icing of the Gurney flap, leading to a smaller difference in moment coefficients in the downwind region. This limited change is consistent with prior findings that Gurney flaps primarily delay trailing-edge separation and improve lift at moderate operating conditions, while added drag and separation sensitivity may emerge as loading increases (Bianchini *et al.*, 2019; Jang *et al.*, 1992).

5. Conclusion

In this study, the impact of icing on vertical-axis wind turbines equipped with Gurney flaps was investigated by coupling blade pitching and sinking motions to emulate operational angle-of-attack fluctuations. Under glaze-icing at 265 K, increasing icing time and tip-speed ratio produced rougher leading edges with horn-shaped accretions; on Gurney-flap (GF) blades, an inverted-triangular accretion formed around the flap with ice concentrated near the tip. Icing weakened the flap's separation-control capability and enlarged trailing-edge vortices, while on the baseline blade the leading-edge horn altered suction-side vortex topology and intensified separation, advancing the azimuth of the torque peak. Consequently, the power coefficient declined with icing duration for both configurations; nevertheless, the GF mitigated performance loss and maintained better output than the baseline at moderate operating conditions (TSR ≤ 3). At higher loading (TSR ≈ 3.5) with prolonged icing (6 min), the GF-VAWT became inoperable. Overall, Gurney flaps can broaden the operable envelope of VAWTs under mild-to-moderate icing, whereas severe icing and high TSR require de/anti-icing measures or operational derating; future work should extend these findings with three-dimensional effects and experimental validation.

References

Balduzzi, F., Bianchini, A., Ferrara, G., et al. (2016). Dimensionless numbers for the assessment of mesh and timestep requirements in CFD simulations of Darrieus wind turbines. *Energy,* 97, 246–261. https://doi.org/10.1016/j.energy.2015.12.111

Bianchini, A., Balduzzi, F., Bachant, P., et al. (2017). Effectiveness of two-dimensional CFD simulations for Darrieus VAWTs: A combined numerical and experimental assessment. *Energy*

Conversion and Management, 136, 318–328. https://doi.org/10.1016/j.enconman.2017.01.026

Bianchini, A., Balduzzi, F., Di Rosa, D., et al. (2019). On the use of Gurney flaps for the aerodynamic performance augmentation of Darrieus wind turbines. *Energy Conversion and Management,* 184, 402–415. https://doi.org/10.1016/j.enconman.2019.01.068

Bianchini, A., Balduzzi, F., Ferrari, L., et al. (2019). On the use of Gurney flaps for the aerodynamic performance enhancement of airfoils and wings. Energy Conversion and Management, 183, 149–164. https://doi.org/10.1016/j.enconman.2018.12.038

Bianchini, A., Balduzzi, F., Ferrari, L., et al. (2019). On the use of Gurney flaps for the aerodynamic performance enhancement of airfoils and wings. Energy Conversion and Management, 183, 149–164. https://doi.org/10.1016/j.enconman.2018.12.038

Bragg, M. B., Broeren, A. P., & Blumenthal, L. A. (2005). Iced-airfoil aerodynamics. Progress in Aerospace Sciences, 41(5), 323–418. https://doi.org/10.1016/j.paerosci.2005.07.001

Brunner, C. E., Kiefer, J., & Hultmark, M. (2022). Comparison of dynamic stall on an airfoil undergoing sinusoidal and VAWT-shaped pitch motions. Journal of Physics: Conference Series, 2265(3), 032006. https://doi.org/10.1088/1742-6596/2265/3/032006

Cole, J. A., Vieira, B. A. O., Coder, J. G., Premi, A., & Maughmer, M. D. (2013). An experimental investigation into the effect of Gurney flaps on various airfoils. Journal of Aircraft, 50(4), 1287–1294. https://doi.org/10.2514/1.C032203

Daróczy, L., Janiga, G., Petrasch, K., Webner, M., & Thévenin, D. (2015). Comparative analysis of turbulence models for the aerodynamic simulation of H-Darrieus rotors. Energy, 90, 680–690. https://doi.org/10.1016/j.energy.2015.07.102

Feng, F., Li, S., Li, Y., et al. (2012). Numerical simulation on the aerodynamic effects of blade icing on small scale straight-bladed VAWT. Physics Procedia, 24, 774–780. https://doi.org/10.1016/j.phpro.2012.02.115

Fouladi, H., Aliaga, C. N., & Habashi, W. G. (2015). Quasi-unsteady icing simulation of an oscillating airfoil. In 7th AIAA Atmospheric and Space Environments Conference (AIAA 2015-3020). https://doi.org/10.2514/6.2015-3020

Fu, Z., & Shi, L. (2016). Aerodynamic performance of wind turbine airfoil under icing condition. Acta Energiae Solaris Sinica, 37(3), 609–616. (In Chinese). https://www.cnki.net

Gao, L., & Hong, J. (2021). Wind turbine performance in natural icing environments: A field characterization. *Cold Regions Science and Technology*, 181, 103193. https://doi.org/10.1016/j.coldregions.2020.103193

Gao, L., Hong, J., & Hu, H. (2021). Wind turbine icing characteristics and icing-induced power losses to utility-scale wind turbines. *Proceedings of the National Academy of Sciences of the United States of America*, 118(41), e2111461118. https://doi.org/10.1073/pnas.2111461118

Islam, M. R., Mekhilef, S., & Saidur, R. (2013). Progress and recent trends of wind energy technology. *Renewable and Sustainable Energy Reviews,* 21, 456–468. https://doi.org/10.1016/j.rser.2013.01.007

Jang, C. S., Ross, J. C., & Cummings, R. M. (1992). Computational evaluation of an airfoil with a Gurney flap. In AIAA 30th Aerospace Sciences Meeting and Exhibit (AIAA Paper 92-2708). Retrieved from https://arc.aiaa.org

Jang, C. S., Ross, J. C., & Cummings, R. M. (1992). Computational evaluation of an airfoil with a Gurney flap. In AIAA 30th Aerospace Sciences Meeting and Exhibit (AIAA Paper 92-2708). Retrieved from https://arc.aiaa.org

Li, S., & Li, Y. (2011). Numerical simulation on icing of a blade aerofoil for vertical axis wind turbines. *Journal of Chinese Society of Power Engineering*, 31(3), 214–219. (In Chinese). https://www.researchgate.net/publication/253086214

Li, Y., Wang, J., & Zhang, P. (2002). Effects of Gurney flaps on a NACA0012 airfoil. Flow, *Turbulence and Combustion*, 68(1), 27–39. https://doi.org/10.1023/A:1015679408150

Lynch, F. T., & Khodadoust, A. (2001). Effects of ice accretions on aircraft aerodynamics. *Progress in Aerospace Sciences,* 37(8), 669–767. https://doi.org/10.1016/S0376-0421(01)00018-5

Manatbayev, R., Baizhuma, Z., Bolegenova, S., et al. (2021). Numerical simulations on static vertical axis wind turbine blade icing. *Renewable Energy*, 170, 997–1007. https://doi.org/10.1016/j.renene.2021.02.023

Martini, F., Contreras Montoya, L. T., & Ilinca, A. (2021). Review of wind turbine icing modelling approaches. *Energies,* 14(16), 5207. https://doi.org/10.3390/en14165207

Mayda, E. A., Van Dam, C. P., & Nakafuji, D. (2005). Computational investigation of finite width microtabs for aerodynamic load control. In 43rd AIAA Aerospace Sciences Meeting and Exhibit. https://doi.org/10.2514/6.2005-1185

McCroskey, W. J. (1981). The phenomenon of dynamic stall (NASA Technical Memorandum 81264). Washington, DC: NASA. Retrieved from https://ntrs.nasa.gov

Rahman, S. O., Azfar, J., Irfan, K. T., et al. (2022). Experimental and numerical evaluation of performance of a variable pitch vertical axis wind turbine. *Journal of Energy Resources Technology,* 144(6), 061303. https://doi.org/10.1115/1.4051896

Reinert, T., Flemming, R. J., Narducci, R., & Aubert, R. J. (2011). Oscillating airfoil icing tests in the NASA Glenn Research Center icing research tunnel. *SAE Technical Paper* 2011-38-0016. https://doi.org/10.4271/2011-38-0016

Rezaeiha, A., Kalkman, I., & Blocken, B. (2018). Towards accurate CFD simulations of vertical axis wind turbines at different tip speed ratios and solidities: Guidelines for azimuthal increment, domain size and convergence. *Energy Conversion and Management*, 156, 301–316. https://doi.org/10.1016/j.enconman.2017.11.026

Rezaeiha, A., Montazeri, H., & Blocken, B. (2018). Towards optimal aerodynamic design of vertical axis wind turbines: Impact of solidity and number of blades. *Energy,* 165, 1129–1148. https://doi.org/10.1016/j.energy.2018.09.192

Rezaeiha, A., Montazeri, H., & Blocken, B. (2019). On the accuracy of turbulence models for CFD simulations of vertical axis wind turbines. *Energy,* 180, 838–857. https://doi.org/10.1016/j.energy.2019.05.053

Son, C., & Kim, T. (2020). Development of an icing simulation code for rotating wind turbines. *Journal of Wind Engineering and Industrial Aerodynamics*, 203, 104239. https://doi.org/10.1016/j.jweia.2020.104239

Syawitri, T. P., Yao, Y.-F., Yao, J., et al. (2020). The effect of Gurney flap on flow characteristics of vertical axis wind turbine. *International Journal of Modern Physics* B, 34(14–16), 2040107. https://doi.org/10.1142/S0217979220401074

Tahir, S. A. R., & Virk, M. S. (2022). Vertical axis wind turbine operation in icing conditions: A review study. *Wind Engineering,* 46(4), 1331–1340. https://doi.org/10.1177/0309524X211061828

Tescione, G., Ragni, D., He, C., Simão Ferreira, C., & van Bussel, G. J. W. (2014). Near wake flow analysis of a vertical axis wind turbine by stereoscopic particle image velocimetry. *Renewable Energy,* 70, 47–61. https://doi.org/10.1016/j.renene.2014.02.042

Tescione, G., Ragni, D., He, C., Simão Ferreira, C., & van Bussel, G. J. W. (2014). PIV-based analysis of 2D and 3D flow phenomena of vertical axis wind turbine aerodynamics. *In 32nd ASME Wind Energy Symposium (AIAA 2014-1080).* Retrieved from https://arc.aiaa.org

Tsai, H. C., & Colonius, T. (2016). Coriolis effect on dynamic stall in a vertical axis wind turbine. *AIAA Journal,* 54(1), 216–226. https://doi.org/10.2514/1.J054199

Wang, J. J., Li, Y. C., & Choi, K. S. (2008). Gurney flap—Lift enhancement, mechanisms and applications. *Progress in Aerospace Sciences,* 44(1), 22–47. https://doi.org/10.1016/j.paerosci.2007.10.001

Wang, Z., & Zhuang, M. (2017). Leading-edge serrations for performance improvement on a vertical-axis wind turbine at low tip-speed-ratios. *Applied Energy*, 208, 1184–1197. https://doi.org/10.1016/j.apenergy.2017.09.012

Xue, W., Luo, G., Zhang, X., et al. (2021). High-resolution numerical simulation of the performance of vertical axis wind turbines in urban area: Part I, wind turbines on the side of single building. *Renewable Energy*, 177, 461–474. https://doi.org/10.1016/j.renene.2021.04.071

Zhang, P., Yang, T., & Lu, X. (2011). Influence of icing pattern on aerodynamic performance of wind turbine airfoils. *Journal of Chinese Society of Power Engineering*, 31(12), 955–973. (In

Chinese). https://www.researchgate.net/publication/289543767

Zhu, H. T., Hao, W. X., Li, C., et al. (2020). Effect of geometry parameters of Gurney flap on the aerodynamic performance of vertical axis wind turbine. *Journal of Engineering for Thermal Energy and Power*, 35(10), 124–130. https://doi.org/10.16146/j.cnki.rndlgc.2020.10.018